PERGAMON

Journal of Atmospheric and Solar-Terrestrial Physics 64 (2002) 451–469

Journal of ATMOSPHERIC AND SOLAR-TERRESTRIAL PHYSICS

www.elsevier.com/locate/jastp

A technical description of atmospheric sounding by GPS occultation

G.A. Hajj *, E.R. Kursinski, L.J. Romans, W.I. Bertiger, S.S. Leroy

Jet Propulsion Laboratory, California Institute of Technology, Mail Stop 238-600, 4800 Oak Grove Dr., Pasadena, CA 91109, USA

Received 10 April 2001; accepted 12 November 2001

Abstract

In recent years, the global positioning system (GPS) has been exploited via radio occultation techniques to obtain profiles of refractivity, temperature, pressure and water vapor in the neutral atmosphere and electron density in the ionosphere. The GPS/MET experiment, which placed a GPS receiver in a low-Earth orbit, provided a wealth of data which was used to test this concept and the accuracy of the retrievals. Several investigations have already demonstrated that the retrieval accuracies obtained with GPS/MET is already comparable, if not better, than the more traditional atmospheric sensing techniques (e.g., radiosondes). Even though the concept of atmospheric profiling via radio occultation is quite a simple one, care must be taken to separate the numerous factors that can affect the occulted signal. These include the motion of the satellites, clock drifts, relativistic effects, the separation of the ionosphere and the neutral atmosphere, and the contribution of the upper atmosphere where sensitivity of the GPS signal is weak. In addition, care must be taken to use proper boundary conditions, use proper smoothing intervals and interpolation schemes to avoid retrieving artificial atmospheric structures, and most importantly detect and correct phase measurement errors introduced by sharp refractivity gradients in the atmosphere. This work describes in some detail the several steps involved in processing such data. In particular, it describes a system that was developed at the Jet Propulsion Laboratory and used to process the GPS/MET data. Several examples of retrieved refractivity, temperature and water vapor profiles are shown and compared to analyses from the European Center for Medium-range Weather Forecast (ECMWF). Statistical comparisons of GPS/MET and ECMWF temperatures for data collected during June 21–July 4, 1995, indicate that differences are of order 1–2 K at northern latitudes where the ECMWF analyses are most accurate.

Keywords: GPS radio occultation; Remote sensing; Refractivity; Temperature; Water vapor; Pressure; Electron density

1. Introduction

The radio occultation technique has three decades of history as a part of NASA's planetary exploration missions (e.g., Fjeldbo and Eshleman, 1969; Fjeldbo et al., 1971; Tyler, 1987; Lindal et al., 1990; Lindal, 1992). Applying the technique to the Earth's atmosphere using the global positioning system (GPS) signal was conceived a decade ago (e.g., Yunck et al., 1988; Gurvich and Krasil'nikova, 1990) and demonstrated for the first time with the GPS/MET experiment in 1995 (Ware et al., 1996). Since then several missions have flown with GPS occultation receivers including Oersted (see, e.g., Escudero et al., 2001), SUNSAT (Mostert and Koekemoer, 1997), CHAMP (see, e.g., Wickert et al., 2001a), and the Argentinian SAC-C (launched in 2000). The promises of the technique have generated much interest from several disciplines including meteorology, climatology and ionospheric physics.

The technique relies on very accurate measurements of the GPS dual-frequency phase delays collected from a receiver in low-Earth orbit (LEO) tracking a GPS satellite setting or rising behind the Earth's atmosphere. The extra phase delay

* Corresponding author. Tel.: +1-818-354-3112; fax: +1-818-393-4965.

E-mail address: george.hajj@jpl.nasa.gov (G.A. Hajj).

1364-6826/02/$ - see front matter
PII: S1364-6826(01)00114-6

induced by the atmosphere can be converted to atmospheric bending which can then be interpreted in terms of refraction due to atmospheric refractivity changes at different heights. Assuming spherical symmetry in the locality of the occulting atmosphere, the index of refraction can therefore be determined from the height of the LEO down to the Earth's surface. Index of refraction can then be converted into electron density above 60 km, neutral atmospheric density, pressure and temperature between 60 km and the middle troposphere, and, with independent knowledge of temperature, into water vapor density in the middle and lower troposphere.

Numerous articles and reports have been written describing the technique, its resolution and accuracy, and its relevance to climate, weather and ionospheric research. On the theoretical front, several papers have addressed the expected resolution and accuracy of the technique (e.g., Gorbunov and Sokolovskiy, 1993; Hajj et al., 1994; Melbourne et al., 1994; Kursinski et al., 1995; Hoeg et al., 1995; Gorbunov, 1996; Gorbunov et al., 1996a,b; Kursinski et al., 1997; Karayel and Hinson, 1997; Mortensen and Hoeg, 1998; Ahmad and Tyler, 1998; Ahmad and Tyler, 1999; Kursinski et al., 2000; Healy, 2001). On the observational front, GPS/MET data have been used to derive temperature, water vapor, geopotential heights of constant pressure levels and ionospheric electron density profiles. GPS/MET-derived temperature profiles agree with those from radiosondes and analyses from the European Center for Medium-range Weather Forecast (ECMWF) to better than 1.5 K between 5 and 30 km altitudes (Hajj et al., 1995; Kursinski et al., 1996; Ware et al., 1996; Rocken et al., 1997; Steiner et al., 1999; Gorbunov and Kornblueh, 2001). Similar results have also been shown from CHAMP (Wickert et al., 2001a). GPS/MET-derived geopotential heights of constant pressure levels agree with those of the ECMWF to $\sim$20 gpm (Leroy, 1997). GPS/MET-derived specific humidities agree with those of the ECMWF to $\sim$0.1 g/kg in the mean (Kursinski and Hajj, 2001). In the ionosphere, GPS/MET data were analyzed to derive electron density profiles in the E and F regions (Hajj and Romans, 1998; Schreiner et al., 1999) and peak electron densities were shown to agree with those of digisondes at the 20% level ($1-\sigma$). In addition, tomographic inversions of GPS/MET and Oersted data were performed to obtain 2-dimensional (2-D) and 3-D images of electron density (Leitinger et al., 1997; Rius et al., 1998; Hajj et al., 2000; Escudero et al., 2001).

Several variations and refinements on the technique of processing GPS radio occultations have been considered in recent years. Those include: (1) inversion of radio occultations using amplitude data (Sokolovskiy, 2000), (2) improved upper stratospheric retrievals (Healy, 2001a,b), (3) improved lower tropospheric tracking and retrievals (Sokolovskiy, 2001a,b), (4) use of radioholographic methods for better handling of atmospheric multipath (Hocke et al., 1999; Gorbunov et al., 2000), use of variational and non-linear optimization approaches for separation of hydrostatic and moist terms in refractivity (Healy and Eyre, 2000; Palmer et al., 2000).

Other studies have considered the use of GPS occultation products in applications such as climate change detection (Yuan et al., 1993; Leroy and North, 2000), numerical weather predictions (Eyre, 1994; Zou et al., 1995; Kuo et al., 1998; Zou et al., 1999; Anthes et al., 2000; Kuo et al., 2000; Zou et al., 2000), and gravity waves morphology (Tsuda et al., 2000; Steiner and Kirchengast, 2000; Hocke and Tsuda, 2001).

The purpose of this paper is to describe in detail a system developed at the Jet Propulsion Laboratory (JPL) for processing GPS radio occultation data to obtain profiles of refractivity, pressure, temperature in the lower neutral atmosphere (below 50 km altitude), water vapor in the middle and lower troposphere, and electron density in the ionosphere. While the technique is conceptually rather simple, there are several issues to be carefully considered in optimally analyzing the data. These issues include the proper calibration of phase delays measured from GPS in order to isolate the atmospheric delay, the detection and correction of measurement errors such as data outages and cycle slips, the proper smoothing of the data and the associated measurement resolution, and the evaluation of errors associated with the estimated atmospheric delay, Doppler shift and bending. The processing steps are illustrated with a specific occultation. Other examples of retrieved refractivity, temperature and water vapor are discussed. Statistical comparisons of GPS/MET and ECMWF temperatures for data collected during June 21–July 5, 1995, are also shown.

The paper is structured as follows. In Section 2 we describe the basics of the GPS signal and how it is modeled. Section 3 describes the process of extracting the atmospheric delay during an occultation and means of detecting and correcting measurement errors. Section 4 describes the inversion process which includes deriving the atmospheric induced Doppler shift and bending, removing the ionospheric effects, the Abel inversion, and then the derivation of the geophysical parameters from refractivity. In Section 5 we present other examples of GPS/MET retrievals and comparisons to the ECMWF analyses. A conclusion is given in Section 6.

2. GPS signal structure and observables

The GPS constellation currently consists of 29 satellites at $\sim$26,500 km radius, $\sim$12 h period, orbiting in six different planes inclined at $\sim$55°. Each GPS satellite broadcasts two signals at L-band ($f_1 = 1575.42$ MHz and $f_2 = 1227.60$ MHz). The L1 and L2 signals received from each GPS satellite can be written as (Spilker, 1980)

$$S_{L1}(t) = \sqrt{2C_{C/A}}D(t)X(t)\sin(2\pi f_1 t + \theta_1) + \sqrt{2C_{P1}}D(t)P(t)\cos(2\pi f_1 t + \theta_1), \quad (1)$$

$$S_{L2}(t) = \sqrt{2C_{P2}}D(t)P(t)\cos(2\pi f_2 t + \theta_2), \quad (2)$$

with

$C_{C/A}$, C_{P1} the received power of the in-phase and quadrature components of the L1 signal, respectively;

C_{P2} the received power of L2;

$D(t)$ an amplitude modulation for L1 and L2 containing navigation data;

$X(t)$ a pseudorandom sequence of ± 1—known as clear acquisition or C/A code—modulating the in-phase component of L1 at a rate of 1.023 Mhz;

$P(t)$ a pseudorandom sequence of ± 1—known as P-code—modulating the quadrature component of L1 and L2 at a rate of 10.23 Mhz.

A properly equipped receiver will detect amplitude, pseudorange [1] and phase measurements for each of the C/A, L1 P-code (P1) and L2 P-code (P2) signals. The C/A and P1 measurements essentially contain identical information, however C/A is preferred over P1 because its power is stronger by 3 dB and is not encrypted. Therefore, the basic observables used during an occultation experiment are the C/A phase and the P2 phase measurements between the low-Earth orbit (LEO) satellite and the occulting GPS satellite. These phase measurements can be modeled (in dimension of distance) as

$$L_k^{ij} \equiv -\frac{c}{f_k}\phi_k^{ij} = \rho^{ij} + \gamma_k^{ij} + C^i + C^j + v_k, \tag{3a}$$

$$\gamma_k^{ij} = \eta_k^{ij} + d\frac{TEC_k^{ij}}{f_k^2}, \tag{3b}$$

with

ϕ_k^{ij} the recorded phase in cycles for the signal propagated from transmitter i to receiver j;

c the speed of light in vacuum;

$k = 1$ or 2 for L1 and L2, respectively;

ρ^{ij} the range corresponding to the travel light time (in vacuum) between the transmitter and the receiver;

γ_k^{ij} the extra delay due to neutral atmosphere and ionosphere;

C^i, C^j time dependent transmitter and receiver clock errors, respectively;

v_k measurement noise which contains the receiver's thermal noise and local multipath.

η_k^{ij} the extra delay due to the neutral atmosphere;

d a constant;

TEC_k^{ij} the integrated electron density along the raypath;

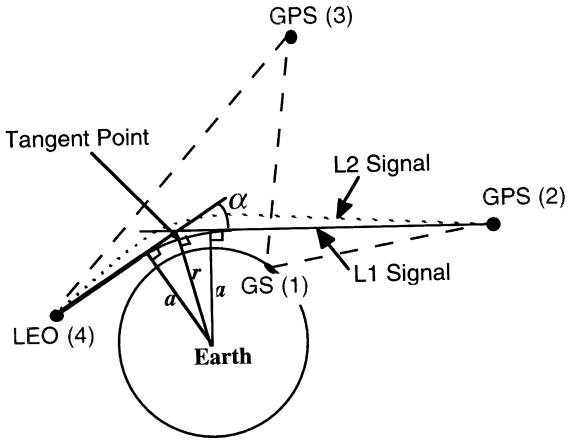

Fig. 1. GPS occultation geometry defining the tangent point, the asymptote miss distance, a, and depicting how the L1 and L2 signals travel slightly different paths due to the dispersive ionosphere. Also shown are the other non-occulting GPS transmitter and ground receiver used for calibration.

Eq. (3a) ignores the following terms:

(1) A bias corresponding to a large integer number of cycles which is constant over a connected arc (i.e., a GPS satellite tracked continuously during the occultation). It is the time derivative of the phase that is of interest to us during an occultation, therefore all additive constants can be ignored.

(2) The "wind-up" term that accounts for the relative orientation of the transmitting and the receiving antennas. Because the geometry and the relative orientation of the transmitting and receiving antennas are well known, this term is modeled and removed (Wu et al., 1993).

(3) Transmitting and receiving antennas phase center variations (which can be calibrated if necessary).

Eq. (3b) ignores higher order ionospheric terms (order $1/f^3$ or higher) which results from the expansion of the Appleton–Hartree formula (see, e.g., Bassiri and Hajj, 1993). This term is normally small, but it becomes a dominant error term at high altitudes (> 40–60 km) during solar-maximum day-time conditions (Kursinski et al., 1997).

Subscripts on any term in Eqs. (3a and b) implies that it depends on the frequency. The neutral atmosphere is non-dispersive at radio frequencies; however, since the electromagnetic signal has to travel through the dispersive ionosphere before and after it reaches the lower neutral atmosphere, the L1 and L2 signals received at a given time sense slightly different parts of the neutral atmosphere (as depicted by the solid, L1, and dotted, L2, occulted signals of Fig. 1). This separation of L1 and L2 signals is the reason to have subscripts on the terms η_k^{ij} and TEC_k^{ij} in Eq. (3b).

[1] Pseudorange is an absolute measurement of group delay between the time a signal is transmitted and received. It is the sum of the actual range between the transmitter and the receiver, atmospheric and ionospheric delays and transmitter and receiver clocks offsets.

3. Isolating atmospheric delay

3.1. The calibration process

Isolating the extra delays induced by the Earth media, γ_k^{ij} and TEC_k^{ij} in Eq. (3b), is the first necessary step toward reconstructing profiles of refractivity. This is accomplished by computing or modeling the clock terms on the right side of Eq. (3a), a procedure that we refer to here as the calibration process.

Depending on the stability of the transmitter's and receiver's clocks, we may or may not need to solve for the clock terms in Eq. (3a). (For the effects of clock instability on atmospheric retrievals, see Kursinski et al., 1997.) For the sake of generality, we will here assume that both the transmitter's and the receiver's clocks are sufficiently unstable and require calibration.[2] In order to be able to solve for both the transmitter's and receiver's clocks, the following geometry is required (see Fig. 1): An occulting receiver (LEO(4)) must view simultaneously an occulting transmitter (GPS(2)) and a non-occulting transmitter (GPS(3)). A second non-occulting receiver (GS(1)) must simultaneously view both the GPS(2) and GPS(3). In order to understand how the calibration of the various clocks is performed we describe in some detail the modeling of the time delay.

We distinguish between three different types of time: (a) clock time, $\hat{t}$, which is the time recorded by the transmitter's or receiver's clock (we call time tag) and contains a time varying offset; (b) proper time, $\bar{t}$, which is the time recorded by a perfect clock in a frame moving with the transmitter or receiver; and (c) coordinate time, t, which is the time recorded by a perfect clock in a given coordinate system. A GPS receiver measures the range between the transmitter and the receiver by essentially differencing the transmitter's time tag associated with a given sequence of code from the receiver's time tag at the time that sequence is received. Up to a constant bias, phase measurements can be thought of in the same manner. Therefore, we can write

$$L^{21} = c(\hat{t}^1 - \hat{t}^2) = c\{(\hat{t}^1 - \bar{t}^1) + (\bar{t}^1 - t^1) + (t^1 - t^2) + (t^2 - \bar{t}^2) + (\bar{t}^2 - \hat{t}^2)\}, \quad (4a)$$

where 1 and 2 corresponds to the id's of the receiver and the transmitter, respectively, as shown in Fig. 1. The difference between the received and transmit time is modeled as the sum of five terms on the right-hand side of Eq. (4a). In their respective order, these terms correspond to the following:

(1) receiver's clock error;
(2) proper time—coordinate time at receiver (due to special and general relativistic effects);
(3) light travel time;
(4) coordinate time—proper time at transmitter;
(5) transmitter's clock error.

Similarly for the other links of Fig. 1 we can write

$$L^{31} = c(\hat{t}^1 - \hat{t}^3) = c\{(\hat{t}^1 - \bar{t}^1) + (\bar{t}^1 - t^1) + (t^1 - t^3) + (t^3 - \bar{t}^3) + (\bar{t}^3 - \hat{t}^3)\}, \quad (4b)$$

$$L^{24} = c(\hat{t}^4 - \hat{t}'^2) = c\{(\hat{t}^4 - \bar{t}^4) + (\bar{t}^4 - t^4) + (t^4 - t'^2) + (t'^2 - \bar{t}'^2) + (\bar{t}'^2 - \hat{t}'^2)\}, \quad (4c)$$

$$L^{34} = c(\hat{t}^4 - \hat{t}'^3) = c\{(\hat{t}^4 - \bar{t}^4) + (\bar{t}^4 - t^4) + (t^4 - t'^3) + (t'^3 - \bar{t}'^3) + (\bar{t}'^3 - \hat{t}'^3)\}. \quad (4d)$$

Under normal operation, for a given receiver time tag, the receiver will record the time delay from all tracked satellites. Therefore, in writing Eqs. (4), L^{21} and L^{31} have the same received time, and similar for L^{24} and L^{34}; but L^{21} and L^{24} have different transmit time ($\hat{t}^2$ and $\hat{t}'^2$, respectively), and similarly for L^{31} and L^{34}, in order to account for the difference in the travel light time. In an occultation geometry, the only term that is of interest to us is the light travel time associated with the L^{24} link, which includes the delay induced on the link by the atmosphere.

In order to obtain $t^4 - t'^2$ we either solve for or compute all the other terms as follows:

(1) Based on knowledge of the positions of both transmitters and receivers (which are obtained from solutions of the orbit using a ground network of GPS stations and all other GPS satellites), we solve for the light time associated with links L^{21}, L^{31} and L^{34} and for the time differences between coordinate and proper times for all links. This is done by accounting for special and general relativistic effects in the manner described by (Wu et al., 1990a) and (Sovers and Border, 1990). Eqs. (5)–(7) summarize their results which is applied to link L^{21} as an example:

The difference between proper time and coordinate time for a receiver fixed on the ground is given by

$$\bar{t}^1 - t^1 = -[(TAI - UTC) + (TDT - TAI)], \quad (5)$$

where TAI-UTC is an integer number of leap seconds which changes approximately once a year and TDT-TAI is defined to be 32.184 s. The travel tight time is given by

$$t^1 - t^2 = \frac{r_{12}}{c} + 2\frac{GM_{\text{Earth}}}{c^3} \ln \frac{r_1 + r_2 + r_{12}}{r_1 + r_2 + r_{12}}, \quad (6)$$

where r_1, r_2, r_{12} are the position of the phase center of the receiver, transmitter and their difference, respectively, in an earth-centered inertial frame; t^2 in Eq. (6) is solved for iteratively given knowledge of the transmitter's orbit. For a transmitter or a receiver in space, the proper and coordinate

[2] This is usually true of the LEO clock and sometime of the GPS clock.

times are related by

$$\frac{d\bar{t}^2}{dt} = \frac{GM_{\text{Earth}}}{c^2 r_2} - \frac{\dot{r}_2^2}{2c^2} + const, \tag{7}$$

where the constant is chosen such that proper and coordinate times agree on the surface of the earth at the equator. Eq. (7) is integrated by standard techniques to give the difference between proper and coordinate times (Wu et al., 1990a).

(2) Given the estimates of $(\bar{t}^1 - t^1), (t^1 - t^2), (t^2 - \bar{t}^2)$ from the previous step, we solve for the drift of clock (2), $(\bar{t}^2 - \hat{t}^2)$, in Eq. (4a) relative to clock (1). Similarly, we solve for $\bar{t}^3 - \hat{t}^3$ in Eq. (4b).

(3) Assuming that clocks (2) and (3) are smooth between samples, we interpolate the corrections obtained in the previous step over the differential light time, therefore we can solve for $\bar{t}'^2 - \hat{t}'^2$ and $\bar{t}'^3 - \hat{t}'^3$.

(4) We solve for $\hat{t}^4 - \bar{t}^4$ in Eq. (4d).

(5) We solve for $t^4 - t'^2$ in Eq. (4c) which is the desired term and corresponds to the first two terms on the right-hand side of Eq. (3a).

Note that in steps (2)–(5) all clock solutions are relative to clock (1), which makes the final solution of step (5) independent of that clock. The only requirement is that clocks be smooth enough between samples for proper interpolation.

For the GPS/MET experiment, the GPS clocks were solved for every 1 s based on 1 s ground measurements and interpolated with a cubic spline to the 50 Hz rate of the receiver. This 1 Hz rate was necessary to solve for the GPS clock variations which were mostly due to selective availability (SA). (SA is the dithering of the GPS clock by the Department of Defense in order to reduce the accuracy for non-authorized users.) After the termination of SA in May of 2000, GPS clock solutions obtained every 30 s or even 5 min can be sufficiently smooth for occultation processing as demonstrated on CHAMP occultations (Wickert et al., 2001b).

The calibration steps described above are performed with GIPSY/OASIS, the software developed at JPL for precise positioning and orbit determination applications using GPS. An example of the atmospheric delay (i.e., γ_k^{ij} in Eq. (3b)) is illustrated in Fig. 2 for an occultation obtained from the GPS/MET experiment. The occultation tangent point are located near 16°S and 171°E geodetic latitude and longitude, respectively. The leveling of the delay at the beginning of the occultation is an indication of where the ionospheric delay is dominant. The atmospheric delay of ~2.4 km near the surface is larger than average; as the water vapor retrieval will later show, this can be attributed to a large moisture concentration.

Another, more straightforward but less accurate, technique (know as "double differencing") is to form the linear combination:

$$L^{24} - L^{34} - (L^{21} - L^{31}) \tag{8}$$

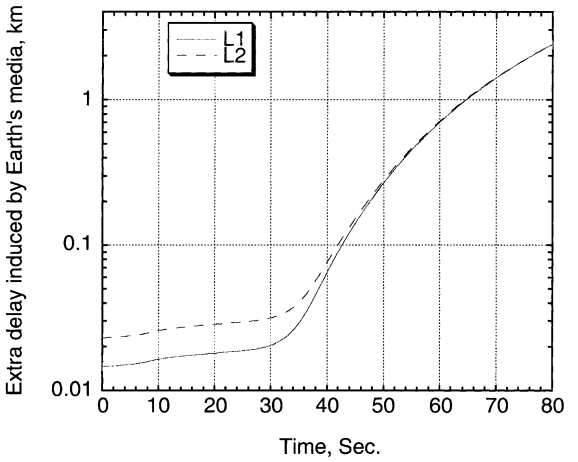

Fig. 2. Extra phase delay induced by the ionosphere and the neutral atmosphere on an occulted signal at 50 Hz rate. The occultation event is between GPS/MET and GPS satellite No. 31. Time 0 corresponds to 1995-6-23:0156.30 UT. The flattening of the curves at the beginning of the occultation is due to the dominant ionospheric delay at these heights.

which causes a number of terms in Eqs. (4) to cancel out. However, only if we ignore clock drifts over the differential light time would all the clock error terms cancel out completely. For a receiver in LEO, the differential light time ranges between 0.01–0.03 s. Prior to the demise of SA, a typical GPS clock drift over a short time scale (seconds–minutes) was of order 6 cm/s (Wu et al., 1990b). Therefore, ignoring the differential light time would introduce an error of 0.5–2 mm of phase measurement. The time variation of this error, which is the relevant number for occultation measurements, depends on the actual spectrum of SA. Fig. 3 shows an example of this error as a function of time during a period when AS was turned on. Even though this error is small (0.1–0.3 mm/s in general), it is not insignificant for retrievals at high altitudes (> 45 km). On the other hand, after SA was terminated, error introduced by the double differencing scheme becomes insignificant at all relevant altitudes.

3.2. Detecting and fixing breaks

In the lower troposphere several effects cause signal tracking to be difficult. These effects include the following: (1) the attenuation of the signal due to defocusing (as discussed later in Section 4 and shown in Fig. 7a). (2) The significant acceleration of the atmospheric phase delay. (3) The scintillation of the signal's amplitude and phase due to diffraction and multipath propagation caused by sharp vertical refractivity gradients. While the first two effects can be easily compensated for by having adequate receiver's antenna gain and proper tracking strategies, the third effect can be

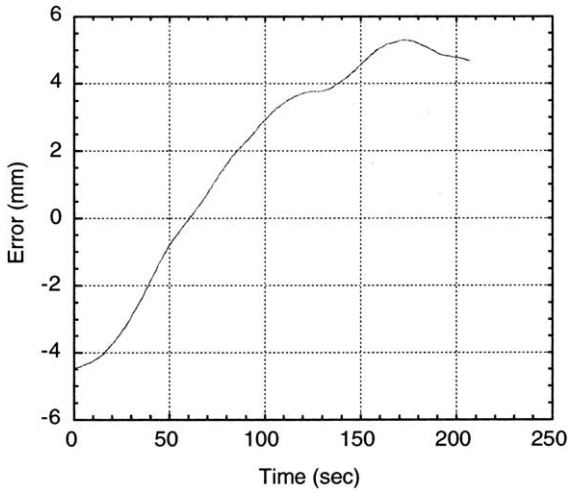

Fig. 3. The error introduced by straight double differencing over the span of an occultation. This is estimated by assuming a differential travel light time of 0.01 s and based on the behavior of the GPS clocks with SA on. This error is eliminated by properly solving for the clocks accounting for the travel light time.

challenging and requires careful examination of the signal's power spectrum to identify the different tones corresponding to different modes of propagation. The examination of the signal's spectrum will take us outside the scope of this paper (however, see Hocke et al., 1999 and Gorbunov et al., 2000). Here, it suffices to say that the GPS receiver used for the GPS/MET experiment was not optimized to handle the complicated dynamics of the signal at the lower troposphere and it only tracked, when possible, the total sum of the multiple signals received at the LEO. During some occultations the effects mentioned above caused the receiver (which tracked at 50 Hz) to (a) slip an integer number of half-cycles at certain time updates, as shown in Fig. 4a, (b) slip a half-cycle at each time update for a certain number of consecutive time updates causing a Doppler shift bias, as shown in Fig. 4b, or (c) loose lock completely.

Figs. 4a and b show examples of these effects. In order to detect half-cycle slips, which are about 10 cm, in delays that are of order 1 km, we examine the unsmoothed Doppler shift obtained by differentiating consecutive phase measurements divided by the time between measurements, Δt (e.g., 0.02 s for GPS/MET). In this procedure a half-cycle corresponds to $1/(2\Delta t)$ Hz (or 25 Hz for GPS/MET). Fig. 4a shows an example of the atmospheric Doppler shift obtained in this manner and detrended by subtracting a second order polynomial fit. In that example we observe two half-cycle slips at 71 and 77 s. Such half-cycle slips are easily fixable.

Additional information on the quality of the data is obtained from the voltage signal-to-noise ratio for each measurement as recorded by the receiver. By definition, the phase thermal noise of a measurement with voltage signal-to-noise ratio of SNR_v is given by $\lambda/(2\pi SNR_v)$,

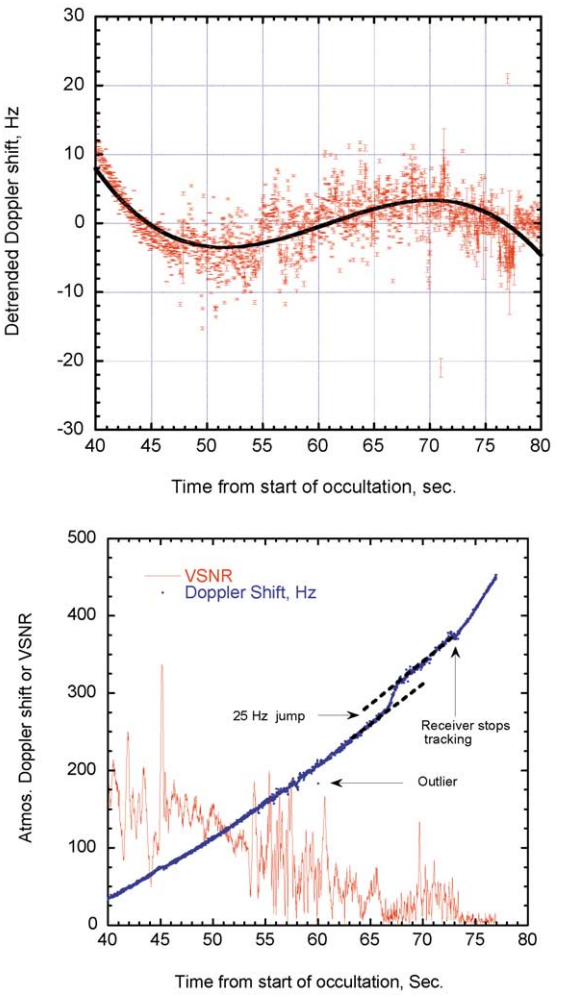

Fig. 4. (Top-a) The atmospheric Doppler shift on the occulted signal corresponding to the occultation of Fig. 2 after subtracting a second order polynomial fit. The Figure shows two outliars at ~71 and ~77 s which correspond to half-cycle slips in the receiver. The error bar are estimated from the signal-to-noise ratio information recorded in the receiver. The solid line is a third order polynomial fit to the data. (Bottom-b) The atmospheric Doppler shift on the occulted signal corresponding to an occultation between GPS/MET-GPS23 starting at 1995-06-23-0031.20 UT. Close examination of the Doppler shift shows: (1) one half-cycle slip at ~60 s, (2) a half-cycle slip at each of the 50 Hz point after ~68 s resulting in the Doppler shift bias of +25 Hz, (3) a change in the slope of the Doppler shift at about 73 s, where the voltage signal-to-noise ratio indicates that the receiver is out-of-lock beyond that point.

where λ is the operating wavelength. Assuming thermal noise to be independent between measurements, the noise on the Doppler shift computed in the manner described above is the root-square-sum of the noise of the two phase measurements used for each point. The error bars indicated in Fig. 4a are obtained in this manner and they help identify

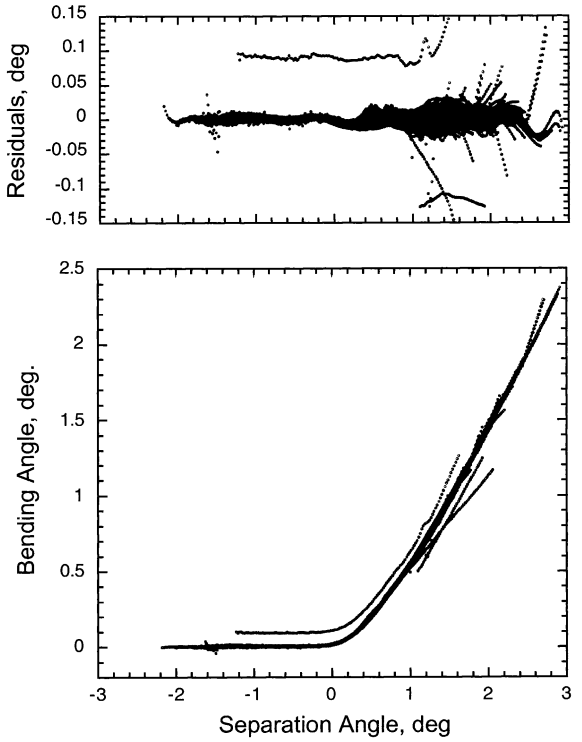

Fig. 5. (Bottom) L1 Bending as function of $(\Omega - \Omega_0)$ for 99 GPS/MET occultations collected on July 2, 1995. Ω is the separation angle between the transmitter and the receiver in a coordinate that represents the local curvature of the Earth near the occultation tangent point (see Fig. 8). Ω_0 is Ω when the tangent point height is at 30 km altitude. (Top) Residual bending after subtracting a 14th order polynomial fit to α_{L1} vs. $(\Omega - \Omega_0)$ in the bottom figure.

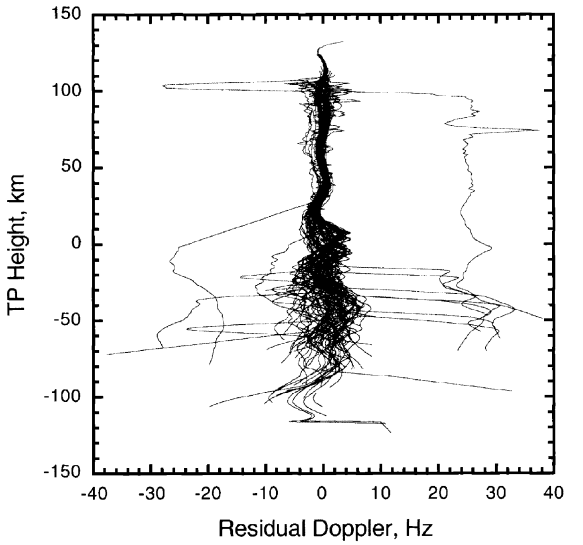

Fig. 6. Residual atmospheric Doppler shift (i.e., measured—predicted) as a function of the occultation tangent height for 85 GPS/MET occultations collected on July 1, 1995. The tangent height is determined based on a straight line connecting the transmitter and the receiver.

when the deviation from the mean Doppler is due to effects other than thermal noise.

Other possible type of biases in the Doppler shift can been seen in Fig. 4b, where, starting at $\sim$68 s past the beginning of the occultation, the Doppler shift is biased by $+25$ Hz relative to the time before 68 s. This is due to a half-cycle slip at each measurement after 68 s. In the example of Fig. 4b, the low voltage signal-to-noise ratio after 73 s indicates that the receiver is no longer in lock.

A systematic method of detecting cycle slips and biases is to subtract a predicted value of the atmospheric Doppler shift from the measured one and examine the residuals. Such a prediction can be obtained by raytracing through an atmospheric model and by knowledge of the geometry of the satellites. However, here we describe a simpler and more direct method of predicting the atmospheric Doppler shift in a manner which is independent of an atmospheric model.

By plotting the L1 bending angle (α_{L1}) estimated from the L1 phase measurements as a function of the separation angle between the transmitter and the receiver (Ω in Fig. 8) for a large number of occultations, we find that they follow very closely the same functional form. (Both α_{L1} and Ω are computed in a coordinate frame that represents the local curvature of the Earth near the occultation tangent point as explained in more detail in Section 4.2.) The bottom panel of Fig. 5 shows α_{L1} vs. $(\Omega - \Omega_0)$ for 99 GPS/MET occultations collected on July 2, 1995, where Ω_0 is the separation angle between the two satellites when the tangent point is at 30 km. The top panel of Fig. 5 shows the residual bending after subtracting a functional form, $F(\Omega - \Omega_0)$, which is a polynomial fit of the 14th order to α_{L1} vs. $(\Omega - \Omega_0)$ in the bottom panel. It should be clear from Fig. 5 that, except for several outliars which are due to improper tracking in the receiver, for any given $(\Omega - \Omega_0)$, α_{L1} can be predicted to within $\pm 0.03^\circ$. Once $F(\Omega - \Omega_0)$ is determined, then, by a process which is the inverse of deriving the bending from the Doppler measurements (described in Section 4.2), the atmospheric Doppler shift can be predicted with an uncertainty of < 10 Hz as seen in Fig. 6. In Fig. 6, the residual atmospheric Doppler (i.e., measured—predicted based on $F(\Omega - \Omega_0)$) for 85 GPS/MET occultations collected on July 1, 1995 are shown as a function of the tangent point height which is computed based on a straight line connecting the transmitter and the receiver.

Once the measured Doppler shift wonders sufficiently far (> 10 Hz) from the prediction, data past that point for that occultation can be eliminated. A similar procedure can be done for L2 data. This provides a systematic and robust manner by which "bad" episodes of an occultation can be detected and discarded.

4. Inversion process

4.1. Deriving atmospheric Doppler

The result of the calibration process is to extract the sum of the neutral atmospheric and ionospheric delays for both the L1 and L2 occulted links. The atmospheric delay is normally obtained at a high rate (50 Hz for the GPS/MET experiment) for the purpose of extracting multipath signals in the lower troposphere, or for sampling the diffraction pattern induced by the atmosphere for high resolution retrievals optics (e.g., Karayel and Hinson, 1997). Our approach is to smooth the high rate data over a period corresponding to the time it takes each signal to cross a Fresnel diameter. The Fresnel diameter of the occulted signal is determined based on L1 and L2 amplitude measurements via the following set of relations:

$$F_0 = \sqrt{\frac{\lambda D_t D_r}{D_t + D_r}}, \tag{9a}$$

$$M = \left[1 - \frac{d\alpha}{dh}\frac{D_t D_r}{D_t + D_r}\right]^{-1}, \tag{9b}$$

$$M = \frac{I}{I_0} = \left(\frac{SNR_v}{SRN_v^0}\right)^2, \tag{9c}$$

$$F = F_0\sqrt{M}, \tag{9d}$$

$$V = V_0 M, \tag{9e}$$

$$T = \frac{2F}{V} = \frac{2F_0}{V_0\sqrt{M}}, \tag{9f}$$

with

F_0, F the first Fresnel zone radius in free space and in Earth atmosphere, respectively;

λ radio link wavelength;

D_t, D_r distance from tangent point to transmitter and receiver, respectively;

M atmospheric scale factor;

α bending due to Earth atmosphere;

$d\alpha/dh$ the derivative of α with respect to the tangent point height;

I_0, I the signal intensity in free space and in Earth atmosphere;

SNR_v^0, SNR_v the instrumental voltage signal-to-noise ratio recorded by the receiver in free space and in Earth atmosphere respectively;

V_0, V vertical velocity of the raypath tangent point in free space and in Earth atmosphere, respectively;

T time to cross a Fresnel diameter in the presence of Earth media.

Knowledge of the satellites' ephemerides allows us to determine F_0 (by use of Eq. (9a)) and V_0. On the other hand, during an occultation, SNR_v is recorded as a function of time, while SNR_v^0 correspond to the SNR_v at the beginning of an occultation. Based on a smoothed version of SNR_v, we compute M according to Eq. (9c) from which we can compute F, V and T via Eqs. (9d–f). The high-rate L1 and L2 phase points are then smoothed over a time interval T with a second-order polynomial fit, and the Doppler shift is derived by taking the time derivative of the fit at the middle of that interval. This smoothing guarantees that diffraction patterns caused by sub-Fresnel atmospheric structure do not appear in the retrieval. However, this procedure does not eliminate ambiguities or errors in determining the Doppler when multiple tones are generated in the atmosphere with tangent point distances larger than the Fresnel zone. This "atmospheric multipath" situation is triggered by sharp changes in refractivity such as around the marine boundary layer causing the occulted signal to travel two or more separate paths connecting the transmitter and the receiver. Identifying the different tones in a multipath situation is a research topic and is not part of our routine processing at this point. In the case of multipath, the smoothing procedure described above will effectively find the average Doppler shift of the different tones.

For the occultation corresponding to Fig. 2, Fig. 7 shows the raw and smoothed L1 SNR_v, the corresponding intensity, Fresnel diameter (which roughly corresponds to the vertical resolution of the measurement), the velocity of the tangent point, and the time it takes the signal to cross a Fresnel diameter. The high concentration of water vapor causes the Fresnel diameter to decrease ($\sim$100 m), the ray tangent point to slow down (the minimum tangent point velocity in Fig. 7b is 10 m/s) at the lowest part of the atmosphere before the signal disappears. The corresponding Doppler shift for this occultation is shown in Fig. 7c.

In order to associate a formal error to the derived Doppler, we consider the following: When averaging over N number of phase measurements, the noise in deriving the slope (which correspond to a Doppler shift) for a linear or second order fit of the phase is given by (see e.g., Bevington, 1969, p. 115)

$$\sigma^2_{\text{Doppler}} = \frac{\sigma_\varphi^2}{\sum t_i^2}, \tag{10}$$

where σ_φ is the standard deviation of a phase measurement (in cycles) assumed to be uncorrelated in time; and t_i is the time of measurement i (for each fit the reference time is set to the middle of the interval). Concentrating on random phase error caused by thermal noise in the receiver, σ_φ is equal to $1/2\pi SNR$ cycles. For large N, with Δ the time between data points (e.g., 20 ms for GPS/MET), we can approximate the sum in the denominator of Eq. (10) by $\Delta^2 N^3/12$ and the error associated with the Doppler estimate is then given by

$$\sigma_{\text{Doppler}} = \frac{a\sigma_\varphi}{\Delta N^{3/2}}, \tag{11}$$

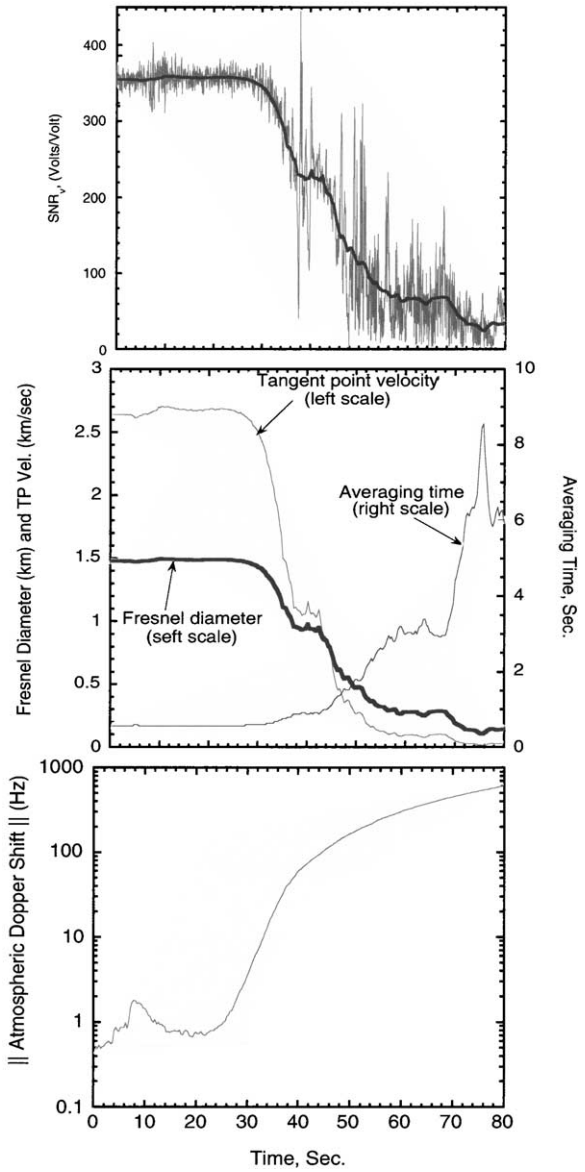

Fig. 7. (Top-a) High rate (thin line) and smoothed (thick line) L1 voltage signal-to-noise ratio for the same occultation event as in Fig. 2. (Middle-b) The Corresponding Fresnel diameter (which sets roughly the vertical resolution), the vertical velocity of the tangent point and the corresponding averaging time of the signal, derived based on Eqs. (9a–f). A running time average with time steps of 0.33 s is used to derive the Doppler shift and bending. (Bottom-c) The absolute value of atmospheric Doppler shift of the occultation. For descending occultations, the atmospheric delay increases with time causing the signal to be blue shifted, therefore the atmosphere introduces a negative Doppler shift. The reverse is true of ascending occultations.

where $a = \sqrt{12}$. (The general form of Eq. (11) is valid for polynomial fit to the data of any order but the value of a changes with the order of the polynomial fit; e.g., $a = 76$ for a third order polynomial.)

We take advantage of this rapid decrease in the Doppler noise with N in order to minimize the noise in the estimated Doppler at high altitudes where the atmosphere is tenuous. For instance, if we desire to reach a specific accuracy σ_{Desired}, then we need to average over N points, where N is given by

$$N \approx \left(\frac{a\sigma_{\varphi}}{\Delta\sigma_{\text{Desired}}} \right)^{2/3}. \tag{12}$$

In practice, when deciding on the appropriate number of phase measurement points to average, we choose the maximum of N (of Eq. (12)) or T/Δ (where T is given by Eq. (9f)). Based on Eq. (11), for an *SNR* of 300 and 1 s averaging, $\sigma_{\text{Doppler}} = 0.0018$ Hz. This would be the Doppler error due to thermal noise if only a single frequency and a single link is used. In reality, two frequencies and four links are used, each contributing its own noise with the L2 being dominant due to its lower *SNR*, making the thermal Doppler noise an order of magnitude bigger. Furthermore, other, usually non-random, sources of error contribute to the Doppler estimate, including orbital velocity errors (~0.01–0.1 mm/s), multipath in the surrounding of one of the two transmitters or two receivers involved in the occultation, and residual ionosphere.

4.2. Deriving atmospheric bending

The atmospheric Doppler shift can be used to derive the atmospheric bending, α, as a function of the asymptotic miss distance, a (Fig. 1). The atmospheric Doppler shift, Δf, can be related to the direction of the transmitted and received signals by the expression

$$\frac{\mathrm{d}\gamma}{\mathrm{d}t} = \lambda\Delta f = [\mathbf{v}_{\mathrm{t}} \cdot \hat{\mathbf{k}}_{\mathrm{t}} - \mathbf{v}_{\mathrm{r}} \cdot \hat{\mathbf{k}}_{\mathrm{r}} - (\mathbf{v}_{\mathrm{t}} - \mathbf{v}_{\mathrm{r}}) \cdot \hat{\mathbf{k}}] \tag{13}$$

with

$\mathbf{v}_{\mathrm{t}}$ and $\mathbf{v}_{\mathrm{r}}$ the transmitter and receiver's velocity, respectively,

$\hat{\mathbf{k}}_{\mathrm{t}}, \hat{\mathbf{k}}_{\mathrm{r}}$ the unit vectors in the direction of the transmitted and received signal, respectively (Fig. 8),

$\hat{\mathbf{k}}$ the unit vector in the direction from the transmitter to the receiver.

Eq. (13) is derived by differencing the Doppler shift observed in the presence of the atmosphere and the Doppler shift that would be observed for the same transmitter–receiver geometry in the absence of the atmosphere. The first-order relativistic contributions to the Doppler are identical in the two situations and cancel out.

Note that this equality is true in general regardless of the shape of the atmosphere; however, Eq. (13) has an infinite number of solutions since $\hat{\mathbf{k}}_{\mathrm{t}}$ and $\hat{\mathbf{k}}_{\mathrm{r}}$ are both unknown, corresponding to four independent parameters. Therefore, certain assumptions have to be made on the shape of the atmosphere in order to derive the atmospheric bending from Eq. (13).

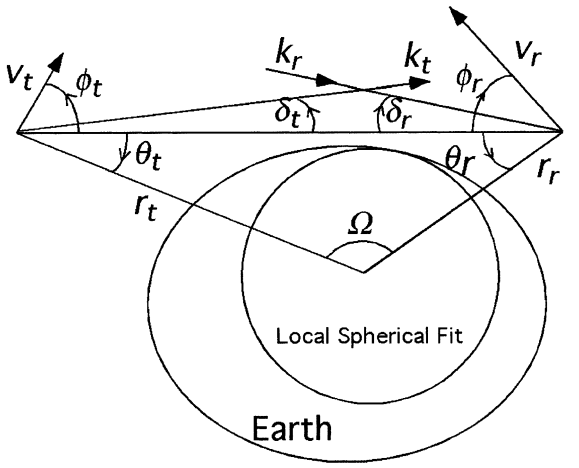

Fig. 8. Occultation geometry defining the angles used in Eqs. (14a and b).

To a very good approximation, the neutral atmosphere is spherically symmetric. In order to account for the ellipticity of the Earth, the center of symmetry is taken to correspond to the circle in the occultation plane which best fits the geoid near the tangent point. The effect of oblateness on radio occultation observations was realized soon after the first such observations of Jupiter's atmosphere were interpreted ignoring oblateness (Kliore et al., 1974, 1975) and yielded temperatures in the deep troposphere several hundred Kelvin hotter than other observations and theory (Eshleman, 1975). Subsequently the average center of curvature as defined by the planet's shape in the vicinity of the tangent point of the occulted ray paths brought the results in line with other observations and theory (Kliore et al., 1976).

Because of the Earth's oblateness, with an equatorial radius roughly 20 km larger than its polar radius, the coordinates used to invert Doppler to bending is adjusted to represent the "local curvature" of the Earth near the occultation tangent point (Fig. 8). This is done as follows: (1) Since the shape of the geoid varies by less than 100 m with respect to an ellipsoid, an ellipsoid can be used to represent the geoid shape. (2) We define an occultation plane which contains the transmitter, the receiver and the normal to the geoid near the tangent point. (Since an occultation may not take place entirely in one plane, this plane is determined by the lowest link of the occultation.) (3) The intersection of the occultation plane and the ellipsoid defines an ellipse. The center of symmetry is taken to be the center of a circle in the occultation plane which is tangent to the ellipse at the ray path tangent point with a radius equal to the ellipse' radius of curvature at the same tangent point. This center is then fixed for the entire occultation, and can be as far as 40 km from the real center of the Earth. Once a center of symmetry is defined, all variables (such as α and a) are defined with respect to that center. Even though this correction to the Earth's center of symmetry has been implemented early on in the GPS occultation processing system at JPL (e.g., Kursinski et al., 1993), a full characterization of the error introduced by ignoring such a correction for GPS occultations was first discussed by Syndegaard (1998).

With the spherical symmetry assumption, Eq. (13) reduces to the equation in two unknowns

$$\frac{\mathrm{d}\gamma}{\mathrm{d}t} = (\mathrm{v_t}\cos(\phi_\mathrm{t} - \delta_\mathrm{t}) - v_\mathrm{r}\cos(\phi_\mathrm{r} - \delta_\mathrm{r})) - (\mathrm{v_t}\cos\phi_\mathrm{t} - \mathrm{v_r}\cos\phi_\mathrm{r}) \quad (14a)$$

(the angles are defined in Fig. 8). In addition, the *formula of Bouguer* (equivalent to Snell's law in a spherically symmetric medium) states that (e.g., Born and Wolf, 1980, p. 123)

$$a = r_\mathrm{t} n_\mathrm{t}\sin(\theta_\mathrm{t} + \delta_\mathrm{t}) = r_\mathrm{r} n_\mathrm{r}\sin(\theta_\mathrm{r} + \delta_\mathrm{r}) \quad (14b)$$

with

$\mathbf{r}_\mathrm{t}, \mathbf{r}_\mathrm{r}$ the vectors from the center of curvature to transmitter and receiver, respectively;

$r_\mathrm{t} = |\mathbf{r}_\mathrm{t}|$;

and $r_\mathrm{r} = |\mathbf{r}_\mathrm{r}|$;

n_t and n_r the indices of refraction at the transmitter and receiver, respectively.

At the heights of the transmitter ($\sim$20,000 km) and receiver (low-Earth orbit), the indices of refraction are assumed equal to 1. This approximation can be shown to introduce a very small error in the estimated bending in the ionosphere (Hajj and Romans, 1998), and it cancels completely after doing the ionospheric calibration to estimate the neutral atmospheric bending. The angles δ_t and δ_r are determined by simultaneously solving Eqs. (14a) and (14b) (easily accomplished using Newton's method and a first guess of $\delta_\mathrm{t} = 0$ and $\delta_\mathrm{r} = 0$). The total bending is $\alpha = \delta_\mathrm{t} + \delta_\mathrm{r}$, and the corresponding a is obtained from Eq. (14b). Fig. 9 shows an example of the bending derived for L1 and L2. The error assigned to the bending is obtained via the simple scaling

$$\sigma_\alpha = \frac{\lambda\sigma_{\mathrm{Doppler}}}{V_0}, \quad (15)$$

where V_0 is the same as in Eq. (9e), and σ_α is given in units of radians.

4.3. Ionospheric calibration

Because of the dispersive nature of the ionosphere, the L1 and L2 links travel along slightly different paths and have slightly different bending (as depicted in Fig. 1). The separation of the two signals at ionospheric heights near the tangent point varies between $<$ 100 m and 5 km, depending on the tangent height of the occulted signal, the solar conditions, local time and the location of the occultation. (For this effect and other ionospheric effects on GPS occultations

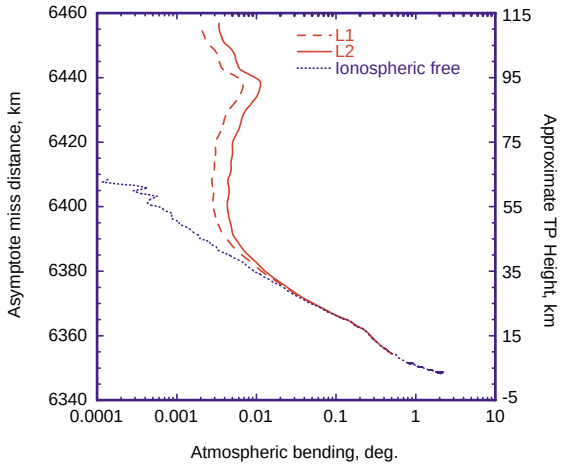

Fig. 9. Estimated total atmospheric bending for L1 and L2, and ionospheric calibrated bending, as a function of a, the asymptote miss distance, for the occultation of Fig. 2. At this stage of the processing, the height of the tangent point is not yet known, but can be approximated as 'a - radius of curvature' and is shown on the right scale.

see, e.g., Hajj and Romans, 1998.) In the most general situation, an ionospheric correction is needed in order to estimate the neutral atmospheric bending. In our approach we follow a procedure first suggested by Vorob'ev and Krasil'nikova (1994). Let $\alpha_1(a_1)$ and $\alpha_2(a_2)$ be the bending as a function of the asymptote miss distance for the L1 and L2 signals, respectively. The linear combination

$$\alpha_{\text{neut}}(a_o) = \frac{f_1^2}{(f_1^2 - f_2^2)}\alpha_1(a_o) - \frac{f_2^2}{(f_1^2 - f_2^2)}\alpha_2(a_o), \qquad (16)$$

where α_1 and α_2 are interpolated to the same value of a_o, removes the first-order ionospheric bending (which is proportional to f^{-2}). The two coefficients on the right-hand side of Eq. (16) have the numerical values to 2.5457… and 1.5457…, respectively.

The interpolation scheme we use is piecewise cubic, within each interval $t_i < t < t_{i+1}$ between data points. The interpolating cubic polynomial $f(t)$ is determined by four conditions fixing the fit and its derivative at the end-points, in terms of the four data values $f_{i-1}, f_i, f_{i+1}, f_{i+2}$. Specifically, the conditions are: $f(t_j) = f_j$ and $f'(t_j) = (f_{j+1} - f_{j-1})/(t_{j+1} - t_{j-1})$ for $j = i, i+1$. This "smooth-cubic" interpolation scheme avoids introducing sharp variations between the points when the data is noisy (in contrast to traditional cubic splines), and is used throughout the remainder of the inversion process (including the Abel transform and the hydrostatic integrals).

Based on Eq. (16), the noise associated with the neutral atmospheric bending is given by

$$\sigma^2_{\alpha_{\text{neut}}} = (2.54)^2\sigma^2_{\alpha_1} + (1.54)^2\sigma^2_{\alpha_2}. \qquad (17)$$

L2 phase measurements are usually noisier than L1 phase measurements for several reasons. First, the L2, which has a lower frequency than L1, is more influenced by ionospheric scintillation and delay. Second, the C/A code is transmitted with 3 dB more power that the P1 code, which in turn is 1–3 dB stronger than the P2. The relative strength of C/A relative to P1 and P2 also depends on whether or not the Department of Defense (DoD) anti-spoofing (AS) is activated, and on the type of the receiver and tracking strategy. In general, L1 phase derived based on C/A is more accurate than L2.

However, even under conditions where both L1 and L2 noise are comparable, Eq. (17) implies that the noise introduced by the ionospheric-free linear combination is about a factor of 3 larger than individual signal noise. We overcome this limitation by redefining the bending in Eq. (16) as

$$\alpha_{\text{neut}}(a_o) = \alpha_1(a_o) + 1.54(\bar{\alpha}_1(a_o) - \bar{\alpha}_2(a_o)), \qquad (18)$$

where $\bar{\alpha}_1$ and $\bar{\alpha}_2$ are the L1 and L2 bending smoothed over longer intervals than discussed in Section 4.2. The longer smoothing interval is normally of order 2 s (100 points of 50 Hz data), which, relative to a Fresnel diameter smoothing (~26 points of 50 Hz data), should correspond to noise about a factor of 7 smaller, according to Eq. (11).

The calibration should not be continued above a certain height, when the neutral atmosphere signature on the occulted signal is comparable to residual ionospheric effects or the receiver's thermal noise. This height is determined by computing a moving χ^2 based on departures from an exponential fit to ionospheric-free bending, and discontinuing the calibration after χ^2 exceeds a specified value. This tends to occur at a height of order ~50–90 km, depending on the ionospheric conditions.

Deeper in the atmosphere, due to defocusing effects and the weakening of the signal, the L2 signal is not used when the SNR_v drops below a certain limit. In that case, an extrapolation of the ionospheric correction (i.e., the term $\bar{\alpha}_1(a_o) - \bar{\alpha}_2(a_o)$ in Eq. (18) is used from higher altitudes to correct for the ionosphere.[3] The ionospheric-free bending for our example occultation is shown in Fig. 9.

For ionospheric retrievals, the bending from one frequency is used above 60 km.

4.4. The Abel inversion

In a spherically symmetric atmosphere, from the formula of Bouguer (Born and Wolf, 1980, p. 123), the signal's bending can be related to the index of refraction via the integral

$$\alpha(a) = -2a\int_a^\infty \frac{1}{\sqrt{a'^2 - a^2}}\frac{\mathrm{d}\ln(n)}{\mathrm{d}a'}\,\mathrm{d}a'. \qquad (19)$$

[3] Extrapolation of the ionospheric correction in this manner was used to generate early results in Kursinski et al. (1996), and also independently suggested and used by Rocken et al. (1997).

This integral equation can then be inverted by using an Abel integral transform given by (see, e.g., Tricomi, 1985, p. 39)

$$\ln(n(a)) = \frac{1}{\pi}\int_a^\infty \frac{\alpha(a')}{\sqrt{a'^2 - a^2}}\,\mathrm{d}a'. \tag{20}$$

The upper limit of the integral in Eq. (19) requires knowledge of the bending as a function of a up to the top of the atmosphere. In practice, however, the estimated bending is reasonably accurate only up to a certain upper height, a_u, as described in Section 4.3. Therefore, in carrying out the integral of Eq. (20) we follow the procedure introduced by Sokolovskiy and Hunt (1996) where we use a least-square estimator of α based on measured bending, α_m, and estimated bending (from an *a priori* model), α_e, weighted by their corresponding uncertainties, $\sigma_m(=\sqrt{\sigma_{\bar{\alpha}_1}^2 + (1.54)^2\sigma_{\bar{\alpha}_1}^2 + (1.54)^2\sigma_{\bar{\alpha}_2}^2}$ based on Eq. (18)) and σ_e. Therefore,

$$\alpha(a) = A(a)\left(\frac{\alpha_m(a)}{\sigma_m^2(a)} + \frac{\alpha_e(a)}{\sigma_e^2(a)}\right),$$
$$A(a) = \left(\frac{1}{\sigma_m^2(a)} + \frac{1}{\sigma_e^2(a)}\right)^{-1}. \tag{21}$$

Since the accuracy of the climatological model is not well known, we choose an adhoc value of $\sigma_e = 0.05\alpha_e$ above a certain height, a_u(=50 km in our example), and $\sigma_e \to \infty$ below a_u. Since refractivity decays exponentially with height, the dependence of the retrieved profile on the climatology used is very small, two scale heights below a_u.

After substituting Eq. (21) in Eq. (20), we obtain

$$\ln(n(a)) = \frac{1}{\pi}\int_a^{a_u} \frac{\alpha_m(a')}{\sqrt{a'^2 - a^2}}\,\mathrm{d}a' + \frac{1}{\pi}\int_{a_u}^\infty \frac{A(a')}{\sigma_m^2(a')} \frac{\alpha_m(a')}{\sqrt{a'^2 - a^2}}\,\mathrm{d}a' + \frac{1}{\pi}\int_{a_u}^\infty \frac{A(a')}{\sigma_e^2(a')}\frac{\alpha_e(a')}{\sqrt{a'^2 - a^2}}\,\mathrm{d}a'. \tag{22}$$

Furthermore, in order to avoid numerically integrating over a weak singularity at the lower boundary of the first integral on the rightside of (22), we rewrite it as

$$\int_a^{a_u} \frac{\alpha_m(a')}{\sqrt{a'^2 - a^2}}\,\mathrm{d}a' = \left[\alpha(a_{int})\ln(a_{int} + \sqrt{a_{int}^2 - a^2}) - \alpha(a)\ln(a) - \int_a^{a_{int}} \ln(a' + \sqrt{a'^2 - a^2})\frac{\mathrm{d}\alpha(a')}{\mathrm{d}a'}\,\mathrm{d}a'\right] + \int_{a_{int}}^{a_u} \frac{\alpha_m(a')}{\sqrt{a'^2 - a^2}}\,\mathrm{d}a' \tag{23}$$

where a_{int} is an intermediate value between a and a_u and is normally chosen to be slightly larger than a. The terms in brackets on the right-hand side of Eq. (23) are the result of integration by parts. Eq. (22) yield the index of refraction, n, as a function of a, at the tangent point (TP). The TP radius is obtained from $r = a/n$. The radius in turn is converted into height above an ellipsoidal fit to the mean sea-level geoid. Fig. 10a shows the retrieved refractivity as a function of height for our occultation example.

We can convert the independent coordinate from height to geopotential height. First we convert all of the tangent point locations into displacements from the center of the Earth. We compute the sum of the gravitational and centrifugal potential energies per unit mass at each position. The gravitational potential energy per unit mass is computed using a version of the JGM-3 gravity model (Tapley et al., 1996). This version is a 64th degree spherical harmonic expansion which can reproduce the mean sea-level geoid with an accuracy of tens of centimeters. The potential of the mean sea-level geoid is subtracted from the sum of the gravitational and centrifugal potentials, and the difference is then divided by a standard value of gravitational acceleration to give the geopotential height. The geopotential height can then substitute for height as the independent coordinate for all derived profiles (Leroy, 1997).

For ionospheric retrievals, the retrieval is performed from 60 km up to the height of the LEO satellite. Above the LEO satellite, the bending is extrapolated with an exponential fit (Hajj and Romans, 1998).

4.5. Deriving geophysical parameters from refractivity

The refractivity, N, is related to geophysical quantities via

$$N = (n-1)\times 10^6 = a_1\frac{P}{T} + a_2\frac{P_w}{T^2} - 40.3\times 10^6\frac{n_e}{f^2} + O\left(\frac{1}{f^3}\right) + a_w W_w + a_i W_i, \tag{24}$$

with

$a_1 = 77.6$ K/mbar;
$a_2 = 3.73\times 10^5$ K^2/mbar;
P total pressure;
T temperature;
P_w water vapor partial pressure;
n_e electron density (m^{-3});
f operating frequency (Hz);
W_w and W_i are liquid water and ice content, respectively, in grams per cubic meter a_s and a_i are 1.4 and 0.6 (cubic meter/grams), respectively.

For realistic suspensions of water or ice, the last two terms of Eq. (24) are small in comparison with other terms and will be neglected here (for discussion of the effects of these terms on GPS occultations see Kursinski, 1997 and Solheim et al., 1999). When the signal is passing through the ionosphere (tangent point height $>$ 60 km), the first two terms

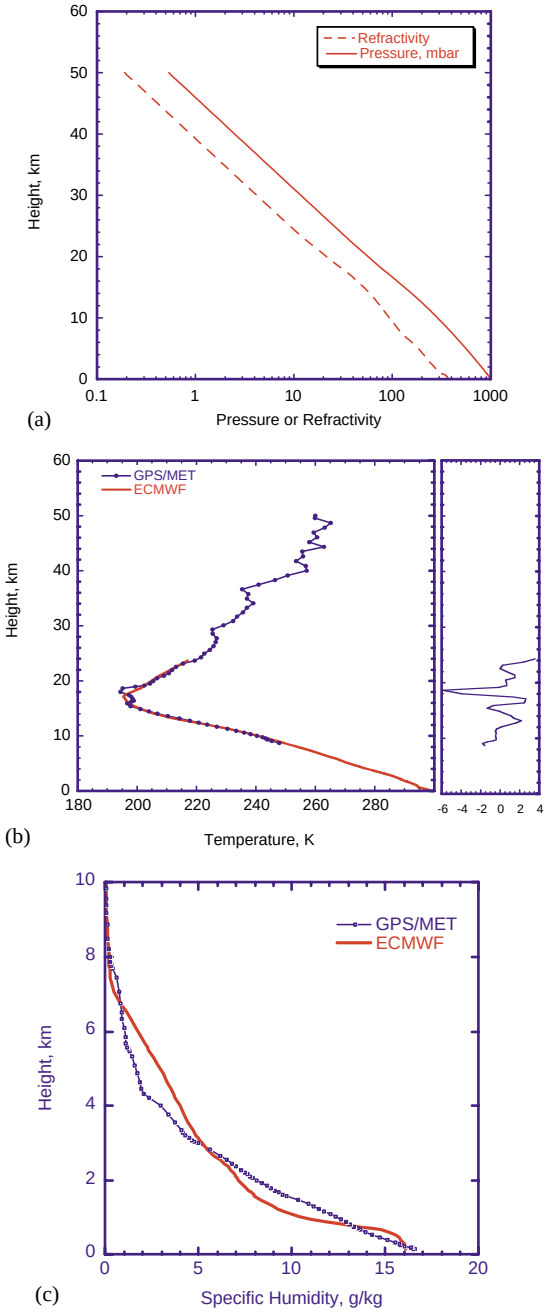

Fig. 10. (a) GPS/MET derived refractivity and pressure. The hydrostatic integral is started at 50 km altitude. (b) GPS/MET and ECMWF analysis temperatures (left) and their differences (right). The ECMWF highest level is at ~23 km. The GPS/MET temperature is retrieved from 50 km down to ~8 km where $T = 250$ K. The agreement is better than 2 K everywhere except near the tropopause, where we ascribe the discrepancy to the model due to insufficient resolution to capture the double tropopause detected from GPS/MET. (c) Specific humidity from GPS/MET and ECMWF analysis. In deriving the GPS/MET specific humidity, the ECMWF analysis temperature was used.

on the right-hand side of Eq. (24) can be ignored, as well as higher order ionospheric terms in the ionosphere. Therefore, measurement of n directly corresponds to electron density in the ionosphere.

In the neutral atmosphere (tangent point height < 60 km), the ionospheric calibration process described in Section 4.3 above effectively removes the first order ionospheric term $(1/f^2)$ in Eq. (24). (Higher order contributions constitute the major source of error during day-time solar maximum at high altitudes; see Kursinski et al., 1997, for an estimate of these errors and Bassiri and Hajj (1994), for possible means of correcting them.) In order to solve for P, T, and/or P_w given N we use the additional constraints of hydrostatic equilibrium and the ideal gas law:

$$\frac{dP}{dh} = -g\rho, \tag{25}$$

$$\rho = \rho_d + \rho_w = \frac{m_d P}{TR} + \frac{(m_w - m_d)P_w}{TR}, \tag{26}$$

with

h height;
g gravitational acceleration;
ρ, ρ_d, ρ_w total, dry air and water vapor densities respectively;
m_d, m_w mean molecular mass of dry air (28.97 g/mole) and water vapor (18.0 g/mole), respectively;
R universal gas constant.

Combining Eqs. (25) and (26), and using Eq. (24) (ignoring the ionospheric terms) to substitute for P/T, we obtain

$$\frac{dP}{dh} = -\frac{gm_d}{a_1 R}N + \frac{a_2 g m_d}{a_1 R}\frac{P_w}{T^2} + \frac{g(m_d - m_w)}{R}\frac{P_w}{T}. \tag{27}$$

Given N, we have a system of two equations (24 and 27) and three unknowns (T, P, and P_w). Since saturation vapor pressure decreases rapidly with decreasing temperature, as dictated by the Clausius–Clapeyron equation, P_w can be ignored above the tropospheric height corresponding to $T = 250$ K; therefore, given N, both T and P can be solved for in the upper troposphere and the stratosphere from Eqs. (24) and (27) and a boundary condition (usually taken to be a temperature boundary condition at ~50 km). The solution to P and T as a function of height for our occultation example are shown in Figs. 10a and 10b, respectively. For comparison, T from the ECMWF nearest 6 hourly analysis and interpolated to the location of the occultation, is also shown in Fig. 10b. Both the GPS/MET and ECMWF analysis temperature agree to better than 2 K everywhere except near the tropopause, where the analysis misses the double tropopause detected by the GPS/MET retrieval.

When P_w is significant, such as in the middle and lower troposphere, it is necessary to have an independent knowledge of one of the three parameters (T, P, P_w) in order to

solve for the other two. Given that temperature is generally better known and less variable than water vapor, it is more efficient to assume knowledge of T, and then solve for P and P_w. The exact relation between errors in T, P and P_w is a function of latitude and height and is described in detail by Kursinski et al. (1995).

Assuming knowledge of $T(h)$ and pressure at some height for a boundary condition, then Eqs. (24) and (27) are solved iteratively as follow:

(1) Assume $P_w(h) = 0$ for a first guess,
(2) Integrate Eq. (27) to obtain $P(h)$,
(3) Use $P(h)$ and $T(h)$ in Eq. (24) to update $P_w(h)$,
(4) repeat steps (2) and (3) until convergence.

Given P and P_w, specific humidity, q (defined as the ratio of water vapor density to the moist air density), is given by

$$q = \left[\frac{m_d}{m_w}\left(\frac{P}{P_w} - 1\right) + 1\right]^{-1} \approx \frac{m_w}{m_d}\frac{P_w}{P}. \quad (28)$$

The solution of specific humidity for our example, using T from the ECMWF analysis, is shown in Fig. 10c. For comparisons, specific humidity from the ECMWF analysis is also shown on Fig. 10c. The retrieved specific humidity at the surface is close to the maximum that is normally observed on Earth. This explains why the delay and bending observations are quite larger than average near the surface.

It is notable that in the occultation example shown the signal was tracked virtually down to the surface, in spite the very large humidity there. The time during which this occultation was taken (June 23, 1995 which is during the second prime GPS/MET period), corresponded to a time where a special tracking software was operating which had improved the tracking in the lower troposphere substantially over the other two prime time periods (for more detail on this see discussion by Kursinski and Hajj, 2001).

5. Examples of GPS/MET retrievals and comparisons to ECMWF

Here, we briefly present other examples of GPS/MET profiles obtained with the system described above, and compare them to corresponding profiles obtained from the nearest 6 h ECMWF analysis interpolated to the location of the occultation.

Fig. 11 shows the results from four different GPS/MET occultation (the three plots aligned horizontally correspond to the same occultation). The date, time, occulting GPS satellite, latitude and longitude of the occultation is indicated at the top of each plot. For each occultation we plot the fractional difference between the GPS/MET and ECMWF refractivity (plots on left), the GPS/MET (solid line) and ECMWF (dashed line) temperatures (middle plots), the GPS/MET (solid line) and ECMWF (dashed line) water vapor pressures (plots on right). These occultations are representative of other occultations obtained during the period of June 21–July 4, 1995, and are chosen to represents different atmospheric conditions (i.e., different latitudes and moisture content).

GPS/MET and ECMWF fractional refractivity plots indicate that refractivity agree to better than 1% in dry regions. Large refractivity differences (up to 6%) appear at lower altitude and can be attributed to differences in moisture. Theoretical estimate indicates that refractivity derived from GPS occultations is accurate to about 1% near the surface and improves at higher latitude (up to ~40 km) (Kursinski et al., 1997).

Statistical comparison of GPS/MET temperature profiles to EMCWF analysis for 579 occultations collected during the period June 21–July 4, 1995 are shown in Fig. 12. These statistics are divided based on the location of the occultations into three regions corresponding to northern (latitude $> 30^\circ$), tropical ($-30^\circ <$ latitude $< 30^\circ$) and southern (latitude $< -30^\circ$) regions. Differences between GPS/MET and ECMWF is ~0.5 K in the mean and ~1.5 K in standard deviation in the northern region. The agreement is worse in the southern region. That this degradation is due to the ECMWF analyses can be concluded based on (1) the fact that GPS/MET retrieval is independent of the region in the globe, (2) the ECMWF analysis is less accurate in the southern hemisphere than in the northern hemisphere due to lack of data. The wavy structure in the tropics around and above the tropopause can be due to gravity waves detected by the GPS/MET but smoothed out by the analysis.

More temperature retrievals obtained from GPS/MET using the described occultation retrieval system as well as statistical comparisons to atmospheric models are discussed by Hajj et al. (1995) and Kursinski et al. (1996). Also retrievals of geopotential height as a function of pressure from GPS/MET and comparison to ECMWF analysis are discussed by Leroy (1997). A detailed water vapor analysis from GPS/MET is given by (Kursinski and Hajj, 2001).

6. Summary/conclusion

We described a system developed at JPL to process GPS occultation data for retrieving refractivity, temperature,

Fig. 11. Retrievals of refractivity, temperature, and water vapor pressure (aligned horizontally for the same occultation) are shown for four different GPS/MET occultations. The date, time, occulting GPS, latitude and longitude of each occultation are indicated on the top of each plot. Retrieved parameters are compared to values derived from the nearest 6 h ECMWF analysis interpolated to the location of the occultation. Fractional refractivity differences between GPS/MET and the analyses are shown on the left. GPS/MET temperatures and water vapor pressures are indicated in solid lines, those of the analysis are indicated in dashed lines. GPS/MET temperatures are shown only above the middle troposphere at a height where $T < 250$ K.

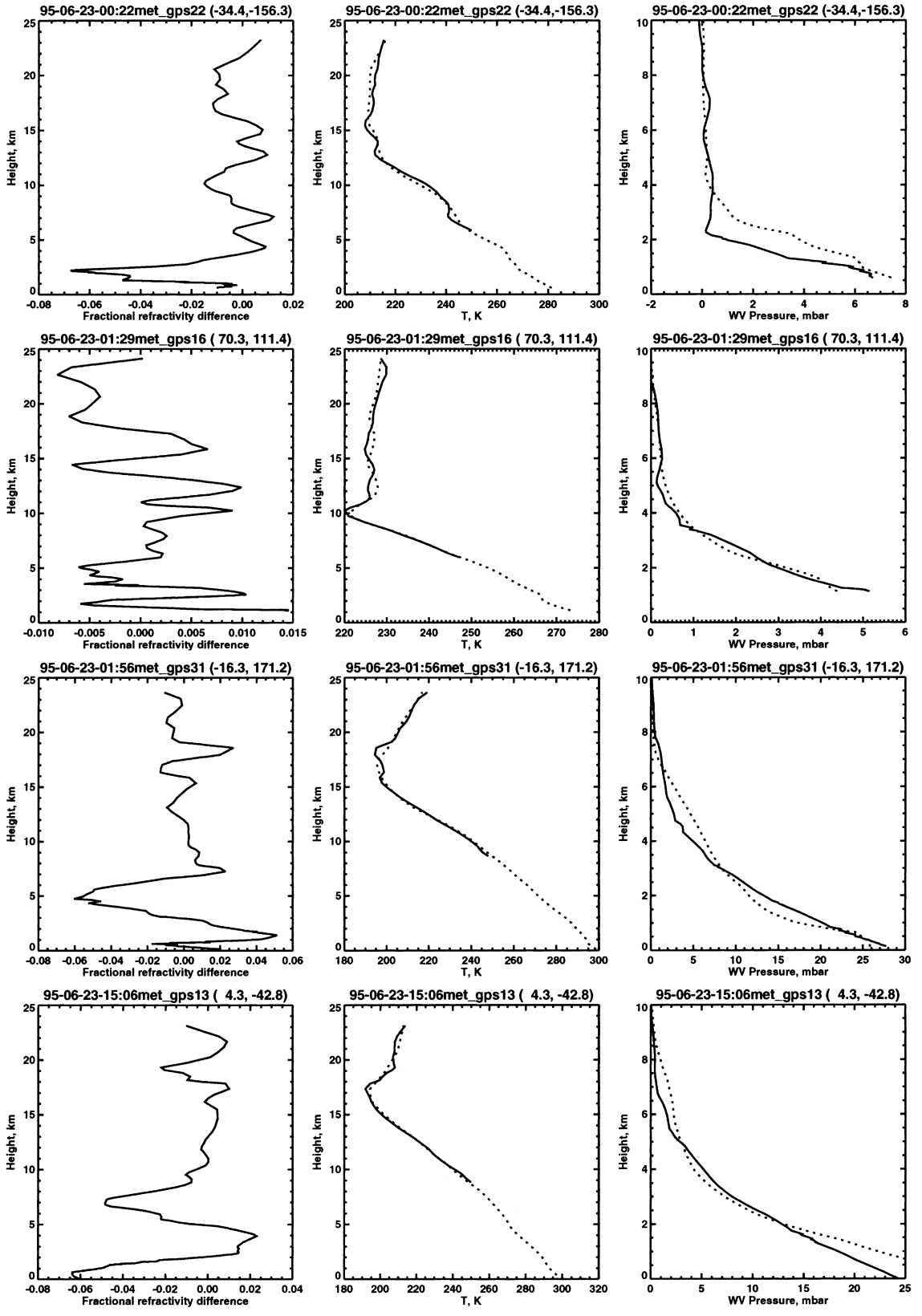
95-06-23-00:22met_gps22 (-34.4,-156.3)
Height, km
Fractional refractivity difference
95-06-23-00:22met_gps22 (-34.4,-156.3)
Height, km
T, K
95-06-23-00:22met_gps22 (-34.4,-156.3)
Height, km
WV Pressure, mbar
95-06-23-01:29met_gps16 (70.3, 111.4)
Height, km
Fractional refractivity difference
95-06-23-01:29met_gps16 (70.3, 111.4)
Height, km
T, K
95-06-23-01:29met_gps16 (70.3, 111.4)
Height, km
WV Pressure, mbar
95-06-23-01:56met_gps31 (-16.3, 171.2)
Height, km
Fractional refractivity difference
95-06-23-01:56met_gps31 (-16.3, 171.2)
Height, km
T, K
95-06-23-01:56met_gps31 (-16.3, 171.2)
Height, km
WV Pressure, mbar
95-06-23-15:06met_gps13 (4.3, -42.8)
Height, km
Fractional refractivity difference
95-06-23-15:06met_gps13 (4.3, -42.8)
Height, km
T, K
95-06-23-15:06met_gps13 (4.3, -42.8)
Height, km
WV Pressure, mbar

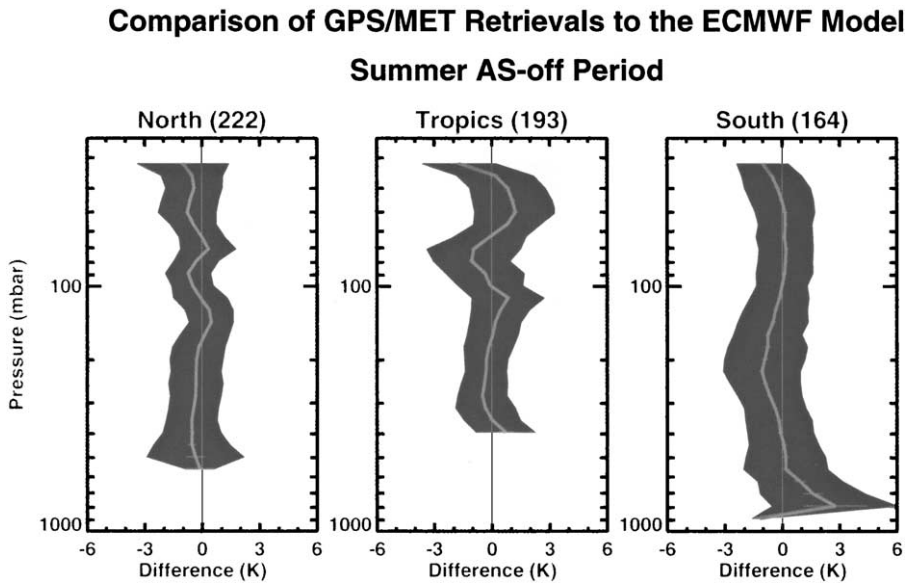

Fig. 12. Statistical comparisons of temperatures derived from GPS/MET and the ECMWF analysis for the period June 21–July 4, 1995. The comparisons is done for three regions: northern mid and high-latitude (>30N), tropical (30S–30N), and mid and high-southern latitudes (>30S). The number of occultations included in the statistics are indicated on the top of each panel.

pressure and geopotential height in the neutral atmosphere and ionospheric free electron density in the ionosphere. Although the concept of radio occultation is a simple one, care must be taken at different steps in the processing of the data in order to obtain accurate retrievals. The system described can be divided into two major parts. First, the calibration of the signal, which implies isolating the atmospheric delay induced on the occulted signal from all other effects such as geometrical motion of the satellites, clocks and ground troposphere. Second, the inversion of the atmospheric delay to obtain physical parameters such as refractivity and other derived products. Our system relies on the most basic approach of using the Abel inversion to obtain refractivity in the atmosphere. More advanced approaches for inverting GPS occultation data include data assimilation into weather models which can be done at different levels, including atmospheric phase delay as a function of time, Doppler shift as a function of time, bending angle as a function of asymptotic miss distance, and refractivity as a function of geopotential height. All of these approaches, however, would still require the first stage of processing, namely, the calibration stage and some ionospheric calibration.

Even though the scope of this work was not to demonstrate how lower tropospheric sensing can be done with GPS on a routine basis, our example demonstrates that it is at least feasible to track the GPS signal down to the surface under very humid conditions. In a future work, we will discuss how lower tropospheric sensing can be obtained at virtually all times with GPS occultation.

Acknowledgements

This work was done at the Jet Propulsion Laboratory of the California Institute of Technology, with funding from the National Aeronautics and Space Agency, Integrated Program Office, and JPL's Director Research Discretionary Funds.

References

Ahmad, B., Tyler, G.L., 1998. The two-dimensional resolution kernel associated with retrieval of ionospheric and atmospheric refractivity profiles by Abelin inversion of adio occultation phase data. Radio Science 33 (1), 129–142.

Ahmad, B., Tyler, G.L., 1999. Systematic errors in atmospheric profiles obtained from Abelian inversion of radio occultation data: effects of large-scale horizontal gradients. Journal of Geophysical Research 104 (D4), 3971–3992.

Anthes, R.A., Rocken, C., Kuo, Y., 2000. Applications of COSMIC to Meteorology and Climate. Terrestrial Atmospheric and Oceanic Science 11 (1), 115–156.

Bassiri, S., Hajj, G.A., 1993. Higher-order ionospheric effects on the Global Positioning System observables and means of modeling them. Manuscripta Geodaetica 18, 280–289.

Bevington, P.R., 1969. Data Reduction and Error Analysis for the Physical Sciences. McGraw-Hill book company, New York.

Born, M., Wolf, E., 1980. Principles of Optics, 6th Edition. Pergamon, Tarrytown, New York.

Escudero, A., Schlesier, A.C., Rius, A., Flores, A., Rubek, F., Larsen, G.B., Syndergaard, S., Hoeg, P., 2001. Ionospheric

tomography using Orsted GPS measurements—Preliminary results. Physics and Chemistry of Earth A 26 (3), 173–176.
Eshleman, V.R., 1975. Jupiterís atmosphere: problems and potential of radio occultation. Science 189, 876–878.
Eyre, J.R., 1994. Assimilation of radio occultation measurements into a numerical weather prediction system. ECMWF Technical Memorandum No. 199.
Fjeldbo, G., Eshleman, V.R., 1969. Atmosphere of Venus as studied with the Mariner 5 dual radio-frequency occultation experiment. Radio Science 4, 879–897.
Fjeldbo, G.F., Eshleman, V.R., Kliore, A.J., 1971. The neutral atmosphere of Venus as studied with the Mariner V radio occultation experiments. Astronomical Journal 76, 123–140.
Gorbunov, M.E., 1996. Three-dimensional satellite refractive tomography of the atmosphere: Numerical-simulation. Radio Science 31, 95–104.
Gorbunov, M.E., Kornblueh, L., 2001. Analysis and validation of GPS/MET radio occultation data. Journal of Geophysical Research 106 (D15), 17,161–17,169.
Gorbunov, M.E., Sokolovskiy, S.V., 1993. Remote sensing of refractivity from space for global observations of atmospheric parameters. Max-Planck-Institute fur Meteorologie Report No. 119, Hamburg, Germany.
Gorbunov, M.E., Sokolovskiy, S.V., Bengtsson, L., 1996a. Space refractive tomography of the atmosphere: modeling of direct and inverse problems. Max-Planck-Inst. Fur Meteorology Report No. 210. Hamburg, F.R. Germany, August.
Gorbunov, M.E., Gurvich, A.S., Bengtsson, L., 1996b. Advanced algorithms of inversion of GPS/MET Satellite data and their application to reconstruction of temperature and humidity. Max-Planck-Institute fur Meteorologie Report No. 211. F.R. Germany, August.
Gorbunov, M.E., Gurvich, A.S., Kornblueh, L., 2000. Comparative analysis of radioholographic methods of processing radio occultation data. Radio Science 35 (4), 1025–1034.
Gurvich, A.S., Krasil'nikova, T.G., 1990. Navigation satellites for radio sensing of the Earth's atmosphere. Soviet Journal of Remote Sensing 7, 1124–1131.
Hajj, G.A., Romans, L.J., 1998. Ionospheric electron density profiles obtained with the global positioning system: results from the GPS/MET experiment. Radio Science 33, 175–190.
Hajj, G.A., Ibanez-Meier, R., Kursinski, E.R., Romans, L.J., 1994. Imaging the ionosphere with the global positioning system. International Journal of Imaging Systems and Technology 5, 174–184.
Hajj, G.A., Kursinski, E.R., Bertiger, W.I., Leroy, S.S., Meehan, T., Romans, L.J., Schofield, J.T., 1995. Initial results of GPS-LEO occultation measurements of Earth's atmosphere obtained with the GPS/MET experiment. Proceedings of the IAG Symposium G1, GPS Trends in Precise Terrestrial, Airborne, and Spaceborne Applications, IUGG XXI General Assy., Boulder, CO, 2–14 July, Springer, Berlin, 1996.
Hajj, G.A., Lee, I.C., Pi, X., Romans, L.J., Schreiner, W.S., Straus, P.R., Wang, C., 2000. COSMIC GPS Ionospheric Sensing and Space Weather. Terrestrial Atmospheric and Oceanic Science 11 (1), 235–272.
Healy, S.B., Eyre, J.R., 2000. Retrieving temperature, water vapour and surface pressure information from refractive-index profiles derived by radio occultation: a simulation study. Quarterly Journal of Royal Meteorological Society 126 (566), 1661–1683.
Healy, S.B., 2001a. Radio occultation bending angle and impact parameter errors caused by horizontal refractive index gradients in the troposphere: a simulation study. Journal of Geophysical Research 106 (D11), 11,875–11,889.
Healy, S.B., 2001b. Smoothing radio occultation bending angles above 40 km. Annals of Geophysics 19 (4), 459–478.
Hocke, K., Tsuda, T., 2001. Gravity waves and ionospheric irregularities over tropical convection zones observed by GPS/MET radio occultation. Geophysical Research Letters 28 (14), 2815–2818.
Hocke, K., Pavelyev, A.G., Yakovlev, O.I., Barthes, L., Jakowski, N., 1999. Radio occultation data analysis by the radioholographic method. Journal of Atmospheric Solar-Terrestrial Physics 61 (15), 1169–1177.
Hoeg, P., Hauchecorne, A., Kirchengast, G., Syndergaard, S., Belloul, B., Leitinger, R., Rothleitner, W., 1995. Derivation of atmospheric properties using radio occultation technique, Scientific Report 95-4, Danish Meteorological Institute, Copenhagen, Denmark.
Karayel, E.T., Hinson, D.P., 1997. Sub-Fresnel-scale vertical resolution in atmospheric profiles from radio occultation. Radio Science 32 (2), 411–423.
Kliore, A.J., Cain, D.L., Fjeldbo, G., Seidel, B.L., Rasool, S.I., 1974. Preliminary results on the atmospheres of Io and Jupiter from the pioneer 10 S-band occultation experiment. Science 183, 323.
Kliore, A.J., Fjeldbo, G., Seidel, B.L., Sesplaukis, T.T., Sweetnam, D.W., Woiceshyn, P.M., 1975. The Atmosphere of Jupiter from the Pioneer 11 S-band Occultation experiment: Preliminary results. Science 188, 474.
Kliore, A.J., Woiceshyn, P.M., Hubbard, W.B., 1976. Temperature of the atmosphere of Jupiter from pioneer 10/11 radio occultations. Geophysical Research Letters 3, 113–116.
Kuo, Y.-H., Zou, X., Huang, W., 1998. The impact of global positioning system data on the prediction of an extratropical cyclone—An observing system simulation experiment. Journal of Dynamics in Atmospheres and Oceans 27, 439–470.
Kuo, Y.-H., Sokolovskiy, S.V., Anthes, R.A., Vandenberghe, F., 2000. Assimilation of GPS radio occultation data for numerical weather prediction. Terrestrial Atmospheric and Oceanic Science 11 (1), 157–186.
Kursinski, E.R., 1997. The GPS radio occultation concept: theoretical performance and initial results. Ph.D. Thesis, California Institute of Technology, Pasadena.
Kursinski, E.R., Hajj, G.A., 2001. A comparison of water vapor derived from GPS occultations and global weather analyses. Journal of Geophysical Research 106 (D1), 1113–1138.
Kursinski, E.R., Hajj, G.A., Hardy, K.R., 1993. Temperature or moisture profiles from radio occultation measurements. Proceedings of the Eighth Symposium on Meteorological Observations and Instrumentation, American Meteorological Society, Anaheim CA, January 17–22, pp. J153–J158.
Kursinski, E.R., Hajj, G.A., Hardy, K.R., Romans, L.J., Schofield, J.T., 1995. Observing tropospheric water vapor by radio occultation using the global positioning system. Geophysical Research Letters 22, 2365–2368.
Kursinski, E.R., Hajj, G.A., Bertiger, W.I., Leroy, S.S., Meehan, T.K., Romans, L.J., Schofield, J.T., McCleese, D.J., Melbourne, W.G., Thornton, C.L., Yunck, T.P., Eyre, J.R., Nagatani, R.N., 1996. Initial results of radio occultation observations of Earth's atmosphere using the global positioning system. Science 271, 1107–1110.
Kursinski, E.R., Hajj, G.A., Hardy, K.R., Schofield, J.T., Linfield, R., 1997. Observing Earth's atmosphere with radio occultation

measurements. Journal of Geophysical Research 102 (D19), 23429–23465.

Kursinski, E.R., Hajj, G.A., Leroy, S.S., Herman, B., 2000. The GPS radio occultation technique. Terrestrial Atmospheric and Oceanic Science 11 (1), 235–272.

Leitinger, R., Ladreiter, H.-P., Kirchengast, G., 1997. Ionosphere tomography with data from satellite reception of Global Navigation Satellite System signals and ground reception of Navy Nav Satellite System signals. Radio Science 32 (4), 1657–1669.

Leroy, S.S., 1997. Measurement of geopotential heights by GPS radio occultation. Journal of Geophysical Research 102, 6971–6986.

Leroy, S.S., North, G.R., 2000. The application of COSMIC data to global change research. Terrestrial Atmospheric and Oceanic Science 11 (1), 235–272.

Lindal, G.F., 1992. The Atmosphere of Neptune: An Analysis of Radio Occultation Data Acquired with Voyager. Astronomical Journal 103, 967–982.

Lindal, G.F., Lyons, J.R., Sweetnam, D.N., Eshleman, V.R., Hinson, D.P., Tyler, G.L., 1990. The atmosphere of Neptune: results of radio occultation measurements with the Voyager 2 spacecraft. Geophysical Research Letters 17, 1733–1736.

Melbourne, W.G., Davis, E.S., Duncan, C.B., Hajj, G.A., Hardy, K.R., Kursinski, E.R., Meehan, T.K., Young, L.E., Yunck, T.P., 1994. The application of spaceborne GPS to atmospheric limb sounding and global change monitoring, JPL Publ. 94-18, Pasadena, California, April.

Mortensen, M.D., Hoeg, P., 1998. Inversion of GPS occultation measurements using fresnel diffraction theory. Geophysical Research Letters 25 (13), 2441–2444.

Mostert, S., Koekemoer, J.A., 1997. The science and engineering payloads and experiments on SUNSAT. Acta Astronautica 41 (4–10), 401–411.

Palmer, P.I., Barnett, J.J., Eyre, J.R., Healy, S.B., 2000. A nonlinear optimal, estimation inverse method for radio occultation measurements of temperature, humidity, and surface pressure. Journal of Geophysical Research 105 (D13), 17513–17526.

Rius, A., Ruffini, G., Romeo, A., 1998. Analysis of ionospheric electron-density distribution from GPS/MET occultations. IEEE Transactions on Geoscience and Remote Sensing 36 (2), 383–394.

Rocken, C., Anthes, R., Exner, M., Hunt, D., Sokolovskiy, S., Ware, R., Gorbunov, M., Schriener, W., Feng, D., Herman, B., Kuo, Y.-H., Zou, X., 1997. Analysis and validation of GPS/MET data in the neutral atmosphere. Journal of Geophysical Research 102 (D25), 29,849–29,866.

Schreiner, W.S., Sokolovskiy, S.S., Rochen, C., Ware, R.H., 1999. Analysis and validation of GPS/MET radio occultation data in the ionosphere. Radio Science 34 (4), 949–966.

Sokolovskiy, S.V., 2000. Inversions of radio occultation amplitude data. Radio Science 35 (1), 97–105.

Sokolovskiy, S.V., 2001a. Modeling and inverting radio occultation signals in the moist troposphere. Radio Science 36 (3), 441–458.

Sokolovskiy, S.V., 2001b. Tracking tropospheric radio occultation signals from low Earth orbit. Radio Science 36 (3), 483–498.

Sokolovskiy, S.V., Hunt, D., 1996. Statistical optimization approach for GPS/MET data inversions. URSI GPS/MET Workshop, Tucson, AZ, February.

Solheim, F.S., Vivekanandan, J., Ware, R.H., Rocken, C., 1999. Propagation delays induced in GPS signals by dry air, water vapor, hydrometeros, and other particulates. Journal of Geophysical Research 104 (D8), 9663–9670.

Sovers, O.J., Border, J.S., 1990. Observation model and parameter partials for the JPL geodetic GPS modeling software "GPSOMC". JPL Publication 87-21, Rev. 2, June.

Spilker, J.J., 1980. GPS signal structure and performance characteristics. In: Janiczek, P.M. (Ed.), Global Positioning System. Institute of Navigation, Washington, DC., pp. 29–54.

Steiner, A.K., Kirchengast, G., 2000. Gravity wave spectra from GPS/MET occultation observations. Journal of Atmospheric and Oceanic Technology 17 (4), 495–503.

Steiner, A.K., Kirchengast, G., Ladreiter, H.P., 1999. Inversion, error analysis, and validation of GPS/MET occultation data. Annals of Geophysics—Atmospheric Hydrology 17, 122–138.

Syndegaard, S., 1998. Modeling the impact of the Earth's oblateness on the retrieval of temperature and pressure profiles from limb sounding. Journal of Atmospheric and Solar-Terrestrial Physics 60 (2), 171–180.

Tapley, B.D., Watkins, M.M., Ries, J.C., Davis, G.W., Eanes, W.J., Poole, S.R., Rim, H.J., Schutz, B.E., Shum, C.K., 1996. The JGM-3 gravity model. Journal of Geophysical Research 101, 28,029–28,049.

Tsuda, T., Nishida, M., Rocken, C., Ware, R.H., 2000. A global morphology of gravity wave activity in the stratosphere revealed by the GPS occultation data (GPS/MET). Journal of Geophysical Research—Atmosphere 105 (D6), 7257–7273.

Tricomi, F.G., 1985. Integral Equations, Dover, Mineola, N.Y.

Tyler, G.L., 1987. Radio propagation experiments in the outer solar system with Voyager. Proceedings of IEEE 75, 1404–1431.

Vorob'ev, V.V., Krasil'nikova, T.G., 1994. Estimation of the accuracy of the atmospheric refractive index recovery from Doppler shift measurements at frequencies used in the NAVSTAR system. Physics of Atmosphere and Ocean 29, 602–609.

Ware, R., Exner, M., Feng, D., Gorbunov, M., Hardy, K., Herman, B., Kuo, Y., Meehan, T., Melbourne, W., Rocken, C., Schreiner, W., Sokolovskiy, S., Solhelim, F., Zou, X., Anthes, R., Businger, S., Trenberth, K., 1996. GPS sounding of the atmosphere from low earth orbit: preliminary results. Bulletin of American Meteorological Society 77 (1), 19–40.

Wickert, J., Reigber, C., Beyerle, G., Konig, R., Marquardt, C., Schmidt, T., Grunwaldt, L., Galas, R., Meehan, T.K., Melbourne, W.G., Hocke, K., 2001a. Atmosphere sounding by GPS radio occultation: first results from CHAMP. Geophysical Research Letters 28 (17), 3263–3266.

Wickert, J., Beyerle, J.G., Hajj, G.A., Schwieger, V., Reigber, C., 2001b. GPS radio occultation with CHAMP: atmospheric profiling utilizing the single difference technique. Geophysical Research Letters, to appear.

Wu, S.C., Bar-Sever, Y., Bassiri, S., Bertiger, W.I., Hajj, G.A., Lichten, S.M., Malla, R.P., Trinkle, B.K., Wu, J.T., 1990a. Global positioning system precision orbit determination sofware design. JPL Publication D-7275, March.

Wu, S.C., Bertiger, W.I., Wu, J.T., 1990b. Minimizing selective availability error on TOPEX GPS measurements, paper presented at the Conference on Astrodynamics. American Institute of Aeronautical and Astronautical/American Astronomical Society, Portland, OR., August 20–22.

Wu, J.T., Wu, S.C., Hajj, G.A., Bertiger, W.I., Lichten, S.M., 1993. Effects of antenna orientation on GPS carrier phase. Manuscripta Geodaetica 18, 91–98.

Yuan, L.L., Anthes, R.A., Ware, R.H., Rocken, C., Bonner, W.D., Bevis, M.G., Businger, S., 1993. Sensing climate change using the global positioning system. Journal of Geophysical Research 98, 14,925–14,937.

Yunck, T.P., Lindal, G.F., Liu, C.H., 1988. The role of GPS in precise earth observation. Paper presented at the IEEE Position, Location and Navigation Symposium, Orlando, FL., November 29–December 2.

Zou, X., Kuo, Y.-H., Guo, Y.R., 1995. Assimilation of atmospheric radio refractivity using a nonhydrostatic adjoint model. Monthly Weather Review 123 (7), 2229–2249.

Zou, X., Vandenberghe, F., Wang, B., Gorbunov, M.E., Kuo, Y.-H., Sokolovskiy, S., Chang, J.C., Sela, J.G., Anthes, R.A., 1999. A ray-tracing operator and its adjoint for the use of GPS/MET refraction angle measurements. Journal of Geophysical Research 104 (D18), 22,301–22,318.

Zou, X., Wang, B., Liu, H., Anthes, R.A., Matsumura, T., Zhu, Y.J., 2000. Use of GPS/MET refraction angles in three-dimensional variational analysis. Quarterly Journal of Royal Meteorological Society 126 (570), 3013–3040.